Coherent Change Detection for High-Resolution Drone-Borne SAR at 24 GHz

Ali Bekar, Muge Bekar, Christopher J. Baker, *Fellow, IEEE*, and Michail Antoniou, *Senior Member, IEEE*

***Abstract*—This article develops and examines techniques to enable coherent change detection (CCD) for short-range, high-resolution drone-borne synthetic aperture radar (SAR) systems operating at high frequencies. The potential of using high frequencies at short ranges for fine-resolution imagery and sensitivity to temporal change detection is highlighted, as are the challenges in terms of sensitivity to SAR motion errors. SAR system characteristics for CCD are derived, and the impact of motion errors, which leads to spatial decorrelation and co-registration errors on CCD maps, is discussed. Subsequently, a CCD algorithm able to generate change maps with a $>$0.75 average coherence value is presented. The validity of the approach is tested through various experimental scenarios. As a result, car tyre marks and human footprints are possible to discern with a drone-borne SAR demonstrator operating at 24 GHz.**

***Index Terms*—Coherent change detection (CCD), drone synthetic aperture radar (SAR), high-resolution imagery.**

I. Introduction

SYNTHETIC aperture radar (SAR) is a coherent imaging technique that can form high-resolution images in any kind of weather or lighting. Spaceborne and airborne platforms have been used in most SAR applications so far. In recent years, drones have started to emerge as an alternative, with different relative merits and drawbacks. In terms of their merits, they are incomparably lower-cost, portable, and simple to deploy without the need for specialized launch infrastructure. Drones are also able to access difficult areas where human access is unsafe/dangerous.

Up to now, several detailed studies have been completed on drone-borne SAR imaging [1], [2], [3], [4], [5], [6], [7], [8], [9], [10], [11], [12]. Drone platforms are especially prone to turbulence during flight, and this is one of the reasons considerable emphasis is given to SAR motion error compensation. In the case of employing low-frequency radars, a high-accuracy dedicated positional system can be enough to compensate for motion errors [1], [2]. On the other hand, when a high-frequency, high-resolution SAR system is used, motion deviations from the nominal trajectory result in high space-variant/invariant phase errors and range walk errors. To compensate for these errors, multistage data-driven autofocus methods are applied with or without drone positional data [5], [6], [7], [8], with potential resolutions in the order of a few centimeters [7], [8]. Using drones as SAR-carrying platforms allows SAR surveys to be conducted at arbitrary temporal baselines, opening new possibilities for monitoring terrain changes with SAR surveys. Already, there are published works on using drone-borne SAR to monitor height changes through differential SAR interferometry, with compact radar systems operating from low frequencies to X-band. For example, the first drone-borne repeat-pass interferogram was obtained using a 10-GHz radar in [5]. However, it was reported that the quality of the interferometric map is not sufficient due to motion errors. In later research, the feasibility of repeat-pass L-band SAR interferometry and SAR tomography was presented in [9]. In [10], crop growth deficit maps were generated by using an L-band drone-borne SAR system. The same SAR system with [10] was used in [11] to predict the sugarcane harvesting date and productivity. In [12], the differential SAR interferometry capability of the L-band drone-borne SAR system was investigated to detect corner reflector displacements. As seen, some repeat-pass interferometry works have been done on low-frequency systems and up to the X-band.

Another major SAR technique that relies on the comparison of repeat-pass, temporally separated SAR images is coherent change detection (CCD) [13]. Spaceborne and airborne SAR change detection have been comprehensively developed and widely used by the SAR community [13], [14], [15], [16], [17], [18], [19]. Nevertheless, this is not yet documented for drone-borne SAR and especially when using the combination of high frequencies and fine resolutions where motion errors are significant for image formation. The previous drone-borne SAR CCD research showed that calibrated target displacements can be detected when motion errors are low [20].

Using higher frequencies increases the sensitivity to subtle changes in the scene. Using high resolution increases synthetic aperture length, leading to a greater likelihood of motion errors. Nevertheless, high-frequency, high-resolution, and short-range SAR application makes CCD more challenging because drone motion instabilities lead to space-variant errors besides space-invariant and range-walk errors. These errors are unique for each pass, which makes two-pass imaging geometries mismatched. Even if two focused SAR images are formed, co-registration errors and spatially invariant/variant phase errors exist in the change map.

Manuscript received 15 August 2023; revised 1 October 2023; accepted 10 October 2023. Date of publication 17 October 2023; date of current version 23 November 2023. The work of Ali Bekar and Muge Bekar was supported by the Ministry of National Education, Türkiye. *(Corresponding author: Ali Bekar.)*

The authors are with the School of Electronic, Electrical and Systems Engineering, University of Birmingham, B15 2TT Birmingham, U.K. (e-mail: alibekar92@gmail.com; mxo748@student.bham.ac.uk; chrisjbaker1@gmail.com; m.antoniou@bham.ac.uk).

Digital Object Identifier 10.1109/JSTARS.2023.3324570

In the article, we investigate the CCD feasibility and potential of high-frequency, high-resolution drone-borne SAR systems and develop an algorithm able to produce change maps by maximizing the coherency of temporally separated image pairs. Several novel features have had to be implemented to achieve robust and well-focused imaging as outlined in the following.

1) The limitations of the drone-borne SAR system that was built are calculated for CCD by evaluating sources of decorrelation. The optimal SAR geometry for change detection operation is also determined.
2) The impact of drone motion errors on CCD using the specified SAR geometry is demonstrated by means of a simulation using trajectories recorded during real-world repeat-pass drone trials.
3) A novel algorithm that allows the detection of subtle changes with a mm-level sensitivity in drone-borne SAR images is proposed. The CCD algorithm includes a data-driven, autofocus-aided drone-borne SAR image formation algorithm, an intensity-based image co-registration algorithm, and a genetic algorithm (GA)-based interferometric phase error compensation method.
4) The performance of the system and the proposed algorithm are validated through several real-world experiments that include different scenarios.

To the best of our knowledge, this is the first consideration of this type of complex system, and while the obtained results show clear potential, we also want to illustrate problem areas/topics that can benefit from dedicated research in the future.

The rest of this article is organized as follows. Section II explains SAR change detection characteristics and the impact of baseline errors on CCD, whereas Section III explains the CCD algorithm. The experimental results are presented in Section IV and the discussion in Section V. Finally, Section VI concludes this article.

II. SAR System Characteristics for CCD

Change detection is fundamentally a repeat-pass, repeat-geometry SAR method. The change itself can be detected by incoherent and coherent methods. In this article, we concentrate on coherent methods measuring the complex correlation between temporally separated images. However, decorrelation sources other than temporal decorrelation may degrade change estimates. This section examines the SAR system based on image decorrelation sources to evaluate the system's limitations and abilities in particular platform motion errors.

A. Coherent Change Detection

There are a few statistical approaches to estimate scatterer changes such as the sample complex cross-correlation method [13], Berger's coherence estimator [16], and log-likelihood clairvoyant detector [17]. In this study, we use the classical coherence estimator given in the following as an initial, first step for drone-borne SAR CCD:

$$CD_C = \frac{\left|\sum_{k=1}^{M} f_k g_k^*\right|}{\sqrt{\sum_{k=1}^{M} |f_k|^2 \sum_{k=1}^{M} |g_k|^2}} \tag{1}$$

where M is the number of resolution cell samples, f and g are the first and the second complex images obtained from two passes, and the symbol $[\cdot]^*$ denotes the complex conjugate.

The coherence estimator output is hereby referred to as a CCD map [16]. The estimation is affected by several decorrelation sources most of which are not associated with an actual scene change. Those are summarized in a seminal paper [21], which the analysis in this section is based on

$$\rho_{\text{tot}} = |\rho_{\text{temp}}| \cdot |\rho_{\text{thermal}}| \cdot |\rho_{\text{spatial}}| \cdot |\rho_{\text{proc}}| \tag{2}$$

where ρ_{tot} is the total correlation, ρ_{temp} is the temporal decorrelation, ρ_{thermal} is the thermal decorrelation, ρ_{spatial} is spatial decorrelation, and ρ_{proc} is processing decorrelation quantifying the decorrelation arising from the algorithms used in image formation and image co-registration.

When there is no thermal noise, temporal change, spatial error, and processing error, the total correlation value between two images would be 1 as stated in (2). We can assume that the images are identical in this instance. If temporal changes are to be measured via (2) all decorrelation sources other than the temporal one should be low enough to generate measurable contrast between the changed and unchanged areas. Then, scene changes can be detected by applying a threshold to the CCD map.

Temporal decorrelation results from scatterer changes between the first and the second acquisitions, and it is given by

$$\rho_{\text{temp}} = \exp\left(-\frac{8\pi^2}{\lambda^2}\left(\sigma_y^2 \sin^2\theta + \sigma_z^2 \cos^2\theta\right)\right) \tag{3}$$

where σ_y is the scatterer's horizontal displacement, σ_z is the scatterer's vertical displacement, and θ is look angle.

Thermal decorrelation can be expressed as a function of signal-to-noise ratio (SNR), and is given as follows:

$$\rho_{\text{thermal}} = \sqrt{\left(\frac{1}{1+\text{SNR}_1^{-1}}\right)\cdot\left(\frac{1}{1+\text{SNR}_2^{-1}}\right)} \tag{4}$$

where SNR_1 and SNR_2 represent the SNR of the receiver during the first and second acquisition, respectively.

If the two imaging geometries are not identical, the spatial decorrelation occurs. By assuming two baselines which are identical with only a constant bias offset between them, the resulting spatial decorrelation can be expressed as follows:

$$\rho_{\text{spatial}} = 1 - \frac{2\cos(\theta_m)\,|\delta\theta|\,d_r}{\lambda} \tag{5}$$

where θ_m is the average look angle of the two-passes, $\delta\theta$ is the look angle difference, d_r is the range resolution, and λ is the wavelength.

As a special case, the total baseline decorrelation is reached in correspondence with the critical baseline, i.e., B_{nc}. When it is orthogonal to the line-of-sight (LOS) of the radar, it can be written as follows:

$$|B_{nc}| = \left|\frac{\lambda R_0 \tan(\theta_m)}{2d_r}\right| \tag{6}$$

where R_0 is the radar to target distance.

Fig. 1. Drone-borne SAR system.

TABLE I
RADAR PARAMETERS OF THE SYSTEM

Centre Frequency	24 GHz
Bandwidth	500 MHz
Azimuth Beamwidth	12.6°
Elevation Beamwidth	76.5°
Tx/Rx Antenna gains	13.2 dBi
Transmit Power	8 dBm
Transmit and Receive Channels	2-Tx, 8-Rx
Noise Figure	~10 dB
System Losses	~3 dB
Weight	0.41 kg

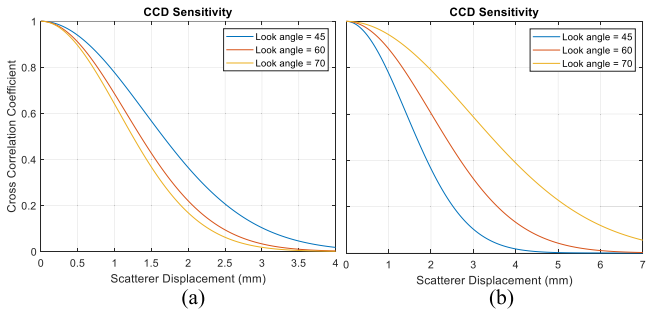

Fig. 2. CCD sensitivity versus (a) horizontal and (b) vertical displacements.

B. Drone-Borne SAR System Evaluation for CCD

Section II-A allows an investigation of de-correlation sources for high-frequency drone-borne SAR and a quantification of their severity. Further investigation is done in this section based on an experimental prototype, using a commercial off-the-shelf radar and a commercial drone as an example. This system was built at the University of Birmingham and is shown in Fig. 1. A DJI M300 drone was used, with an onboard INRAS Radarbook operating at 24 GHz [7]. The radar parameters are representative of conventional automotive-type radars, as given in Table I.

The capabilities and limitations of CCD using high-frequency drone-borne SAR are evaluated next, based on (3)–(6) and Table I. Fig. 2 shows the temporal decorrelation (3) observed by the system in Table I, for different horizontal and vertical displacements. This, in turn, specifies CCD sensitivity limits. As indicated, the SAR system has mm-level sensitivity. For example, at a 60° look angle, a horizontal scatterer displacement of 1.5 mm results in a correlation of 40%. Higher look angles are more sensitive to horizontal changes whereas low look angles have a better sensitivity to vertical changes, as (3) also suggests.

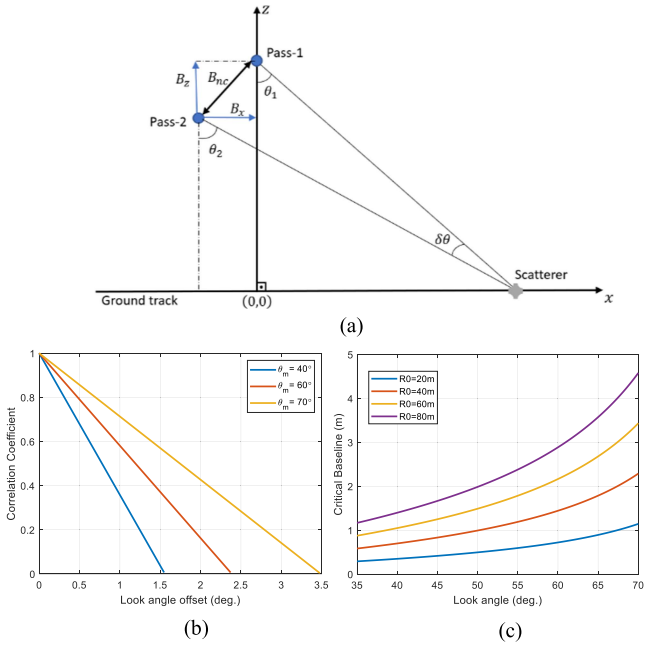

Fig. 3. (a) Two-pass SAR geometry with a constant bias offset. (b) Spatial decorrelation due to the look angle offset. (c) Critical baseline which is orthogonal to LOS of the radar.

Thermal decorrelation is related to SNR as given in (4). Previous work [7] shows that the image sensitivity for the considered radar system parameters is almost 30 dB when the range to the target area is around 70 m. Hence, the thermal decorrelation can be negligible at short ranges.

In Fig. 3(a), two-pass SAR geometry with a constant bias offset between them is shown. The spatial decorrelation due to the constant look angle offset is plotted for different average look angles by using (5) in Fig. 3(b). As expected, the correlation coefficient decreases as the look angle offset increases and lower average look angles are more sensitive to the angular offset. In Fig. 3(c), the critical baseline, which is orthogonal to the LOS of the radar, is plotted against the average look angle for different target range values R_0 based on (6). For example, when the range to the target is 60 m, we have a 1-m critical baseline value at a 40° average look angle (the corresponding angular offset is around 1.5°), and a 2.7-m baseline value at a 65° look angle (the corresponding angular offset is around 2.5°). Higher average look angles increase the critical baseline value. Similarly, higher range values make the critical baseline greater. However, it is worth noting that the maximum transmit power of this type of radar is low (8 dBm or similar), so a bigger range value may cause a reduction in SAR image sensitivity. Also, it increases the required aperture length to achieve the desired azimuth resolution, hence motion error can be more severe in the aperture. Therefore, choosing an acceptable R_0 is significant. From experimentation, the baseline which is orthogonal to the LOS of the radar is less than 1.5 m in most cases. Examination of Fig. 3 shows that ranges higher than 40 m, look angles of around 60° can provide image correlation for a 1.5 m baseline. Also,

the vicinity of 60° look angle provides average sensitivities to both horizontal and vertical changes as illustrated in Fig. 2.

C. Motion Error Impact on Decorrelation

In the previous section, the effect of a constant baseline offset on spatial decorrelation is examined. On the other hand, in a realistic scenario, the relative difference in the paths followed has constant, linear, and nonlinear components. Here, we will examine the impact of the drone's motion deviations on decorrelation. When there is a relative difference in the paths followed, decorrelation arises between the image pair. Drones as a SAR platform, operating at close range and prone to motion deviations, can exaggerate this effect. Providing an analytical derivation with a closed-form solution to describe this problem is difficult due to the dependence on drone trajectories and used algorithms. However, we can present a method to numerically compute it and a numerical example based on our parameters to illustrate the severity of the problem. In this section, a CDD simulation is done by using an example pair of a drone's real, recorded positional data to illustrate the actual impact of the motion errors on the CCD result. These data were acquired from a drone attempting to repeat the same trajectory twice, with a temporal separation of less than 20 min, under good weather conditions.

In the simulation, all decorrelation sources other than spatial are ignored. A hypothetical SAR system with the parameters shown in Table I is considered. The range to the target area center was assumed as approximately 42 m, whereas the look angle to the center point of the image was adjusted to 63° to fulfill the specifications given in Section II-B. The scene dimensions were assumed as 10 m by 15 m, with the scene comprising uniformly distributed uncorrelated scatterers. It was further assumed that a set of 60 scattering centers are located randomly within a resolution cell whose size is 0.3 m in range and 0.1 m in the cross-range direction. Also, 4-point like targets were placed in the scene to prove the resolution and allow error-free co-registration of the image pair. The scene size was kept relatively small to minimize space-variant phase errors within each individual image. In Fig. 4(a), the experimental scenario is shown, and the recorded positional data within one radar beam are shown for two flights in Fig. 4(b). The constant bias offset between the passes is only in the order of a few cm in this example. Hence, this constant shift along the horizontal and vertical axes does not cause significant decorrelation on the CCD map for this scenario. Nonetheless, linear, and nonlinear errors may still degrade the CCD map although they are relatively low in this scenario.

In the simulation, the nonlinear phase errors shown in Fig. 5(a) and (b) were calculated based on the scene center and artificially compensated to mimic a perfect autofocus routine. Then, images from each acquisition were formed by using the conventional range-Doppler algorithm [22] and co-registered using the positional data via an affine transformation [23]. The final images are shown in Fig. 5(c) and (d). Calculating cross-correlation coefficients using (1) and a sliding window of 2×6 pixels ($M = 12$), the result shown in Fig. 6 is obtained. If

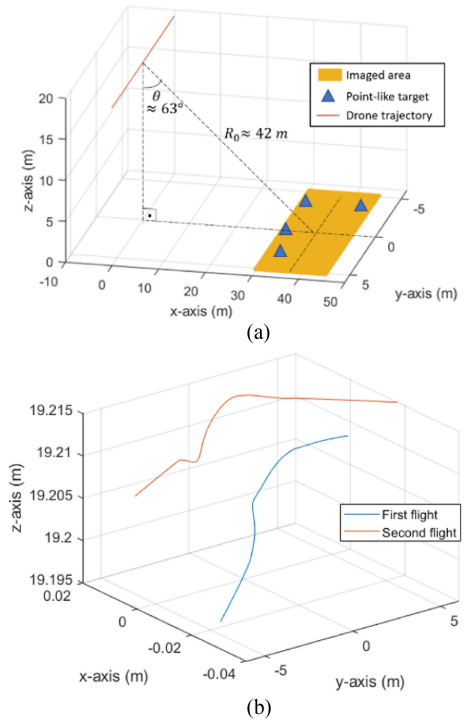

Fig. 4. (a) Simulation scenario. (b) Two-pass positional record. Blue: first track. Red: second track.

there were no phase errors, the phase of the change map would have a unit phase value, and the change map would show a correlation of 100%. On the other hand, the residual phase error is nonlinear and the resulting coherence map exhibits a loss of coherency that is spatially variant across the target area, even for the limited scene size and relatively low motion errors of this example, and with almost total loss of coherency in some parts [see Fig. 6(b)]. As nonlinear space-invariant phase errors were compensated, the existing errors must result from constant, linear, and space-variant nonlinear phase errors. However, in a real-world scenario, a perfect autofocus and a high-accuracy co-registration routine cannot be assumed, so residual phase errors resulting from these processes would contribute to decorrelation. Hence, phase errors induced by the motion errors and processing errors should be removed from the map to be able to observe subtle changes repeatedly and robustly. In the next section, an algorithm is proposed to address this problem.

III. Change Detection Algorithm

The algorithm includes two main modules (see Fig. 7). In the first, two-pass radar raw data are processed to form high-resolution focused images. In drone-borne SAR, high deviations from the nominal trajectory that result in range walk errors and spatially variant/invariant phase errors are common, making the use of motion compensation techniques necessary. The image formation process followed is the same as in [8] and is briefly mentioned here for the sake of completeness. The algorithm flow chart is shown in Fig. 8.

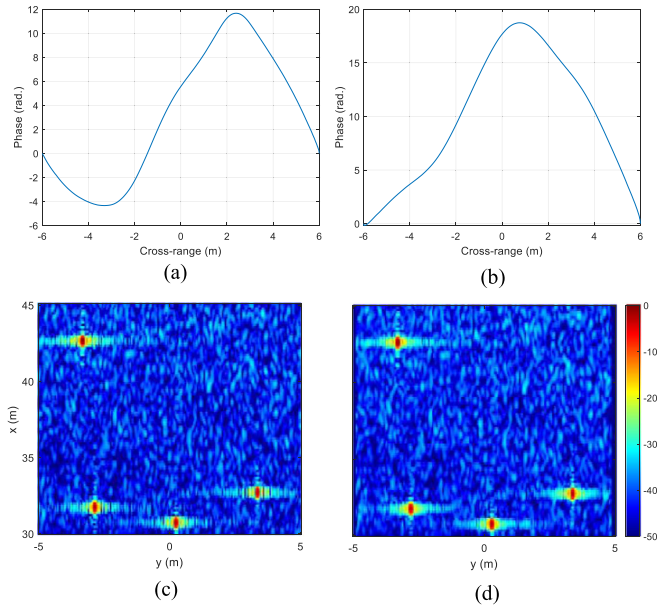

Fig. 5. (a) First flight nonlinear phase error. (b) Second flight nonlinear phase error. (c) Formed image from the first acquisition and (d) formed image from the second acquisition, where the *x*-axis represents the ground range, and the *y*-axis represents the cross-range.

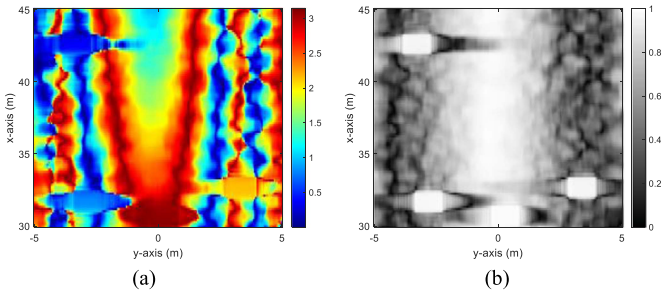

Fig. 6. (a) CCD phase and (b) CCD magnitude, where the *x*-axis represents the ground range, and the *y*-axis represents the cross-range.

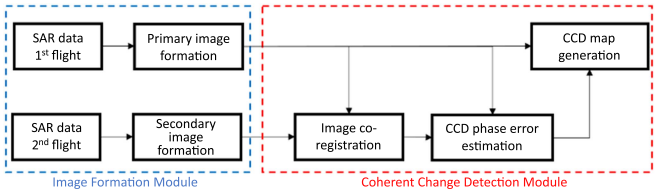

Fig. 7. Change detection algorithm.

In the image formation module, range-walk errors are corrected before the range compression, whereas phase errors are compensated in the range-frequency, azimuth-time domain as

$$\tilde{s}\left(f_r,u\right)=\left(\int_{-\frac{T_m}{2}}^{\frac{T_m}{2}} x_s\left(t,u\right)\ e^{-j2\pi f_r t}dt\right)\ e^{j\emptyset_{er}(u)} \tag{7}$$

where $x_s(t,u)\ =(\int_a^b s(f_r,u)e^{j2\pi f_r t}df_r\ )\ e^{(j\frac{\emptyset_{er}(u)\gamma}{f_c}\ t)}$, a and b are minimum and maximum range frequencies, $s(f_r,u)$ is the range compressed SAR data, f_r is range frequency, T_m is sweep time, t is fast-time, u is slow time, f_c is operating frequency, γ is chirp rate, $\tilde{s}(f_r,u)$ represents the error-corrected range-compressed data, and $\emptyset_{er}(u)$ is the phase error function formed by the motion compensation (MoCo)/autofocus algorithms.

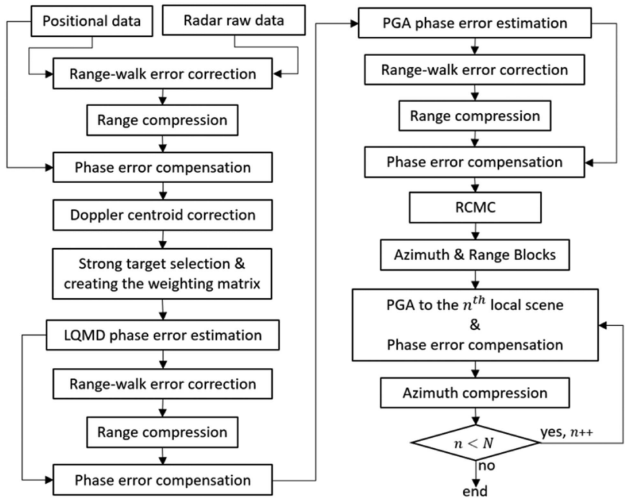

Fig. 8. Image formation algorithm.

As illustrated in Fig. 8, after positional data-based MoCo, the Doppler centroid is adjusted to zero, and strong targets are selected to perform autofocus. Then, the space invariant errors are estimated by local quadratic map-drift (LQMD) and phase gradient algorithm (PGA), respectively. After space invariant error correction, range cell migration correction (RCMC) is applied, and N local scenes are created by dividing the image into azimuth and range blocks. Overlapped or nonoverlapped local scenes can be created. Then, PGA is implemented in each block to minimize space-variant errors. The SAR data that contains each block can be expressed as

$$s_c\left(f_r,u\right)=\left[s_{\mathrm{LS}_1},\ s_{\mathrm{LS}_2},\ldots,s_{\mathrm{LS}_N}\right] \tag{8}$$

where $s_c(f_r,u)$ is the data before the azimuth compression, s_{LS_n} is the nth $(\mathrm{n}\ =\ 1,\ 2,\ldots,N)$ phase error corrected local scene.

In this work, azimuth compression is done for each local scene separately. The Fourier transform of the local scene, i.e., $S_{\mathrm{LS}_n}(f_r,f_a)$, is multiplied by the Fourier transform of the reference function, i.e., $H(f_r,f_a)$. By taking the inverse Fourier transform of this multiplication, the focused local image is generated as

$$S_{\mathrm{LS}_n}\left(f_r,u\right)\ =\int_{-\frac{f_{\mathrm{PRF}}}{2}}^{\frac{f_{\mathrm{PRF}}}{2}} s_{LS_n}\left(f_r,f_a\right)\cdot H\left(f_r,f_a\right)e^{j2\pi f_a u}\,df_a \tag{9}$$

where $H(f_r,f_a)\ =\int_{-\frac{u_a}{2}}^{\frac{u_a}{2}} e^{j\pi\frac{2v^2u^2}{\lambda r}}\cdot e^{-j2\pi f_a u}\,du$, v is the platform speed, r is slant range, f_a is azimuth frequency, and u_a is the acquisition time for the corresponding local scene.

The local image $S_{\mathrm{LS}_n}(x,y)$ is formed on the xy-plane after converting the slant range into the ground range.

The image formation process is identical for both primary ("primary") and repeat-pass ("secondary") radar data. As a

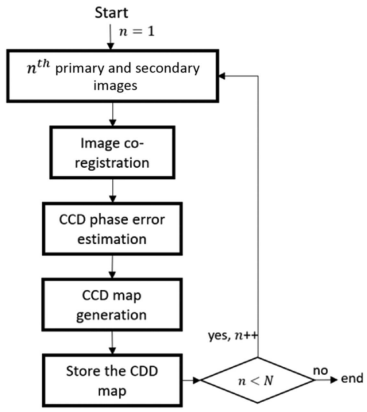

Fig. 9. CCD module.

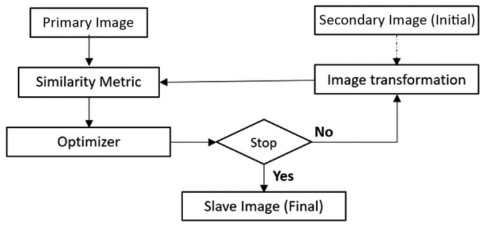

Fig. 10. Intensity-based image co-registration.

next step, the formed primary and secondary local images $S_{\mathrm{MLS}_n}(x, y)$ and $S_{\mathrm{SLS}_n}(x, y)$ are sent to the CCD module.

As it can be seen in Fig. 7, the CCD module includes three main blocks: image co-registration; CCD phase error compensation; and CCD map generation. The process is explained in detail in the following to provide a better understanding of the CCD process. The detailed flowchart of the CCD module is given in Fig. 9.

A. Image Co-Registration

In this stage, the secondary image is aligned with the primary image by geometrically modifying it. There are intensity-based and feature-based registration methods [24]. As an initial attempt, we use the intensity-based image registration approach. This approach seeks the maximum similarity of intensity patterns between the images by modifying the geometrical transformation matrix iteratively. The main steps of the algorithm are shown in Fig. 10.

The image transformation matrix $\boldsymbol{A}$ is given as

$$\boldsymbol{A} = [c_1\ c_2\ 0; c_3\ c_4\ 0; c_5\ c_6\ 1\ ] \tag{10}$$

where $c_i\ (i = 1, 2, \ldots, 6)$ are the coefficients to be determined.

The new position of the pixel at the coordinates (x, y) after the transformation applied is given by

$$(x', y') = (c_1 \cdot x + c_2 \cdot y + c_5,\ c_3 \cdot x + c_4 \cdot y + c_6\ ). \tag{11}$$

To move the corresponding pixel to its new position, the image is interpolated. This transformation corrects registration errors resulting from translation, rotation, scale, and shear. In the initial step, c_1 and c_4 are set to 1, whereas others are 0 for the secondary image to remain unchanged. After the secondary image modification, the similarity of the secondary image and the primary image is calculated using mutual information (MI) which is a measure of how much information the secondary image provides about the primary image [25], [26], [27]. MI, i.e., $I(S_{\mathrm{MLS}_n}, S_{\mathrm{SLS}_n})$, is calculated using the marginal probabilities $p(m)$ and $p(s)$, and the joint probability $p(m, s)$ where m and s are intensity bins of the primary and secondary images, respectively. It is given by

$$I\left(S_{\mathrm{MLS}_n}, S_{\mathrm{SLS}_n}\right) = \sum_{m,s} p\left(m, s\right) \ln\left(\frac{p\left(m, s\right)}{p\left(m\right) p\left(s\right)}\right). \tag{12}$$

As the MI is maximized, the secondary image aligns correctly with the primary image [25]. After obtaining the similarity metric, the coefficients of the image transformation matrix (10) are optimized by using an evolutionary optimizer as detailed in [28] to maximize MI. This process is repeated iteratively until the algorithm reaches the maximum number of iterations or the desired similarity value. In this way, the geometrically aligned secondary image $\tilde{S}_{\mathrm{SLS}_n}(x, y)$ is obtained.

B. Phase Error Estimation and CCD Map Generation

In most cases, the primary image $S_{\mathrm{MLS}_n}(x, y)$ and the co-registered secondary image $\tilde{S}_{\mathrm{SLS}_n}(x, y)$ contain residual constant, linear, and nonlinear phase errors due to imperfect MoCo and digital processing. As shown in Section II-C, these errors cause time-varying baseline errors and loss of coherency that is spatially variant across the target area while some of them (e.g., constant, and linear errors) cannot fundamentally be corrected by autofocus methods.

If the CCD phase error at point (x, y) is $\emptyset_{\mathrm{err}}(x, y)$, the phase error-free, the coherence map is given as follows based on (1):

$$\Lambda_{\mathrm{CCD}}\left(x, y\right) = \left| \frac{\sum_{g=1}^{G} S_{\mathrm{MLS}_n}\left(g\right) \tilde{S}_{\mathrm{SLS}_n}\left(g\right)^{*} \exp\left(-j\emptyset_{\mathrm{err}}\left(g\right)\right)}{\sqrt{\sum_{g=1}^{G} \left|S_{\mathrm{MLS}_n}\left(g\right)\right|^2 \sum_{g=1}^{G} \left|\tilde{S}_{\mathrm{SLS}_n}\left(g\right)\right|^2}} \right| \tag{13}$$

where Λ_{CCD} is the coherence map, G is the total number of resolution cells, and g represents the pixel located at point (x, y), with values from 1 to G.

$\emptyset_{\mathrm{err}}$ is the unknown quantity and should be estimated. To aid its estimation, $\emptyset_{\mathrm{err}}$ can be expressed as a polynomial of some order. Conducting a dedicated study for drone-based systems is a complex problem, so as a first step, we rely on the existing literature. Specifically, here we use the model in [29]. This was originally developed to remove phase distortions due to flat Earth and topographic effects in space-borne SAR interferometry. As will be shown in Section IV, the model given with the following equation can be used to form acceptable coherence maps when the scene size is kept small although some residual phase errors remain in the map:

$$\emptyset_{\mathrm{err}}\left(x, y\right) = w_0 + w_1 x + w_2 y + w_3 xy + w_4 x^2 + w_5 y^2 \tag{14}$$

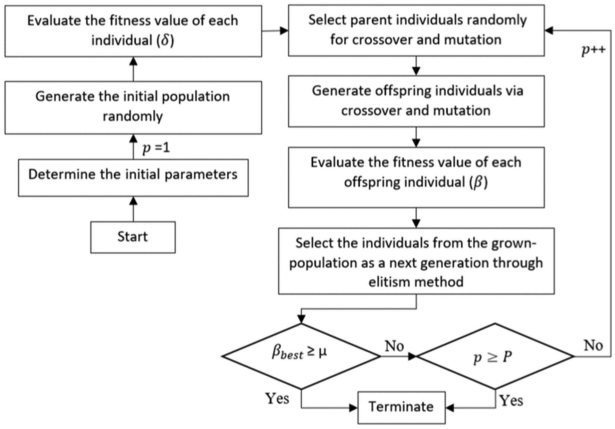

Fig. 11. Genetic algorithm.

where w_i $(i = 0, 1, \ldots, 5)$ are the coefficients to be determined.

The coefficients may be obtained by implementing least-squares as in [30]. However, the method needs pixel selection from the unchanged area in time between the flights. In this work, we employ a GA-based optimization technique [31] to estimate the coefficients of the CCD phase error function (14). This technique does not require any particular pixel selection and is able to compensate for CCD phase errors globally within the change map. The main steps of GA to find the coefficients are demonstrated in Fig. 11. In the first step, initial parameters are determined such as the number of individuals in the initial population, number of maximum generation (P), number of cross-overs, mutation rate of each gene, desired average coherency (μ), and possible solution range of each phase error coefficient.

Based on initial parameters, the first population is generated, and the fitness value of each individual, which is the average value of (13), i.e., β, is evaluated. Then, a group of individuals is selected for crossover and mutation, and offspring—new individuals are generated. As a next step, the β value of each new individual is evaluated. With regard to the selection part, as many individuals as in the initial population are selected from the existing population, and few of them must have the best coherency and other individuals can be chosen randomly—this method is called elitism [32]. In the final step, if the best individual (β_{best}) is equal or bigger than μ or the generation number (p) reaches P, the algorithm is terminated, otherwise, the algorithm repeats itself from the parent selection part by increasing the generation number.

After obtaining the error function, $\emptyset_{\text{err}}(x, y)$ from GA, the local change map is formed using (13). By repeating these steps for all local scenes, the full map is formed as shown in Fig. 9.

IV. Experimental Verification and Performance Assessment

An experimental campaign was carried out to verify the algorithms in Section III and to experimentally assess their performance. Experiments were carried out at the University of Birmingham Metchley Lane sport pitches. The ground was covered by 2.5-cm-long grass. Several corner reflectors were spread throughout the target area for georeferencing purposes and to assess algorithm outcomes with or without scene changes. 40-m-long SAR apertures were generated by flying the drone at an altitude of roughly 20 m with approximately 3 m/s velocity. In total, 32 flights were collected for different scenarios on the same day. The experiment site can be seen in Fig. 12(a). Here, two different scenarios extracted from 4 different flights are considered to show the capability of the SAR system and validate the proposed radar system concept. The first one is human footprint detection whereas the second includes a standing person and a car track with turns.

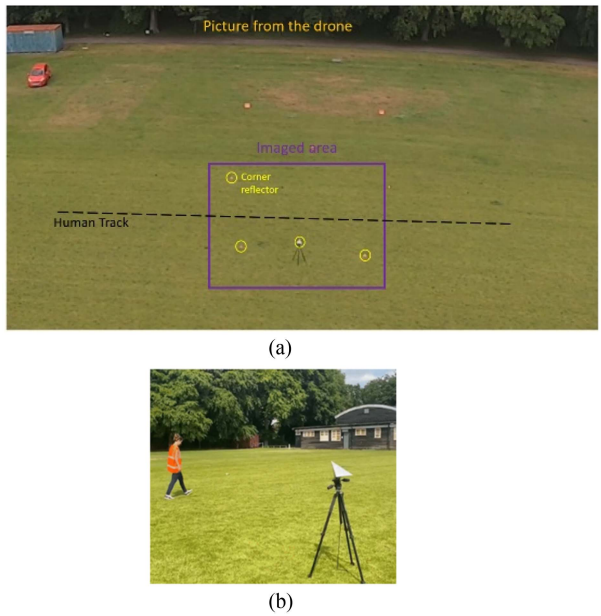

(a)

(b)

Fig. 12. First scenario. (a) Scene. (b) Walking person after the first flight.

A. Scenario I

In this scenario, the first drone-borne SAR data were collected before making any changes to the scene. The second SAR data were collected after a person walked on the grass at normal speed. The human track can be seen in Fig. 12(a), whereas the walking person's photo is in Fig. 12(b). The total azimuth length of the radar data collected was 40 m, whereas the scene size along the ground-range direction was 32 m. The processing begins with the positional data-based MoCo as mentioned in Section III. The recorded positional data of the two tracks are shown in Fig. 13. The constant horizontal baseline offset was around 0.7 m whereas the constant vertical baseline offset was 0.06 m according to the recorded positional data. However, it is worth keeping in mind that the positional data accuracy is between ± 0.5 m.

As described in Section III, the Doppler centroid is adjusted to zero before the space invariant MoCo is implemented, which is based on LQMD and PGA. Strong target selection was based on corner reflectors placed in the scene. After space invariant MoCo, RCMC is applied, and the images are divided into four azimuth and two range blocks. Then, another PGA is

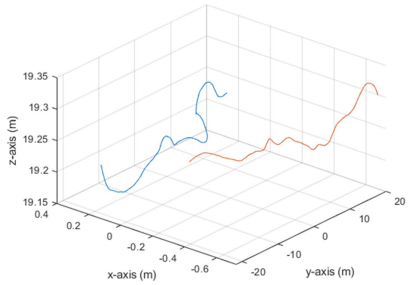

Fig. 13. Positional data of the two tracks—the first track is in blue, and the second track is in red.

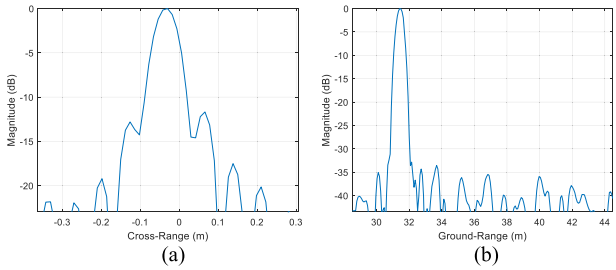

Fig. 15. Cross-section of the corner-reflector shown in the yellow rectangle in Fig. 14(c). (a) Cross-range profile. (b) Ground-range profile.

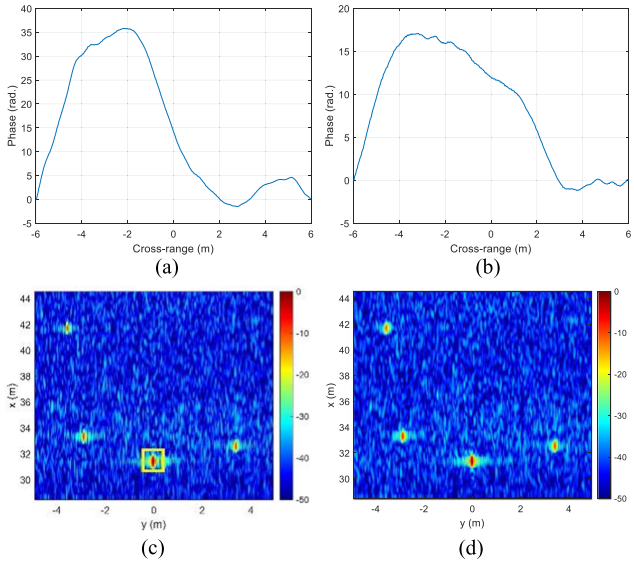

Fig. 14. (a) Total estimated phase error for the primary image. (b) Total estimated phase error for the secondary image. (c) Formed primary image. (d) Co-registered secondary image.

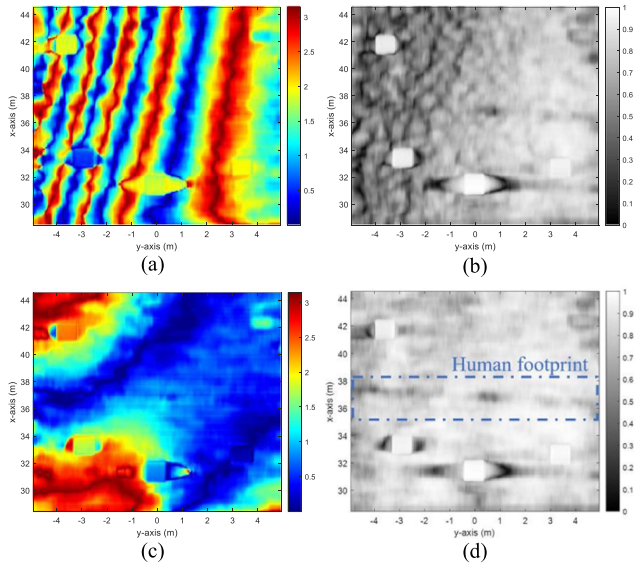

Fig. 16. (a) CCD phase before GA-based optimization. (b) CCD map before GA-based optimization. (c) CCD phase after GA-based optimization. (d) CCD map after GA-based optimization.

implemented in each subimage. In this way, space-variant errors are minimized in the subimages. Here, we focus on only one subimage shown in the purple rectangle in Fig. 12(a). Similar to the simulation in Section II-C, there are 4 corner reflectors in the scene, and the size of the scene is 10 m $\times$ 16 m. Fig. 14(a) and (b) shows the summed phase errors of the space-invariant and space-variant estimations for the interested subimage. The primary and the secondary images are formed with a 6 cm azimuth and 40 cm ground-range resolution. The range and cross-range profile of the target shown in the yellow rectangle in Fig. 14(c) are shown in Fig. 15(a) and (b), respectively. The next step is to co-register the primary and the secondary images. The primary image and the co-registered secondary image can be seen in Fig. 14(c) and (d), respectively. At this point, if the cross-correlation coefficients are calculated by using a 2 $\times$ 8 sliding window, Fig. 16(a) and (b) is obtained. The phase of the change map can be seen in Fig. 16(a). The change map has a 0.6 average coherence with a significant decorrelation on the left side [see Fig. 16(b)]. This degradation is caused by the residual phase errors denoted by $\emptyset_{\text{err}}$ in Section III-B. As described in that section, $\emptyset_{\text{err}}$ can be assumed as a polynomial function, and its coefficients can be estimated iteratively by a GA-based optimization method (see Section III-B). In GA, the number of cross-overs are selected empirically as 25, whereas the mutation rate of each gene is 0.005. Also, the desired average coherency is decided as 0.95. The possible solution range of each phase error coefficient was empirically chosen as ± 20 for w_1 and w_2, ± 1 for w_3, and ± 0.5 for w_4 and w_5. w_0 has no impact on the coherence map, so it was ignored. The phase error is estimated by creating 30 generations that each include 50 individuals. Fig. 17 shows how GA maximizes the coherency of the change map. In the figure, the horizontal axis represents the number of generations created, whereas the vertical axis represents the fitness value β, which is the average value of (13). The mean fitness value of each generation is shown in blue, whereas the individual who has the best fitness value in each generation is shown in red.

As indicated, the best fitness value is obtained in the 21st generation with a 0.81 average coherence. The formed coherence map and phase are shown in Fig. 16(c) and (d). The human footprint can be seen clearly in Fig. 16(d) and has a correlation coefficient of 0.65 (average). In this figure, the decorrelation on the right and left side of the corner reflectors is due to the high sidelobes of the reflectors seen in Fig. 14(c) and (d).

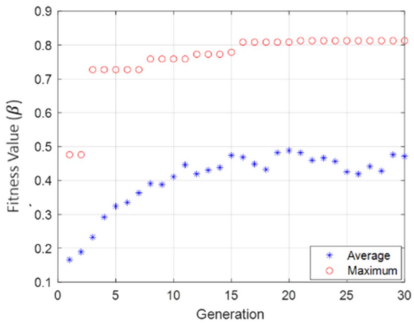

Fig. 17. GA processing: The mean fitness value of each generation is shown in blue and the individual who has the best fitness value in each generation is shown in red color.

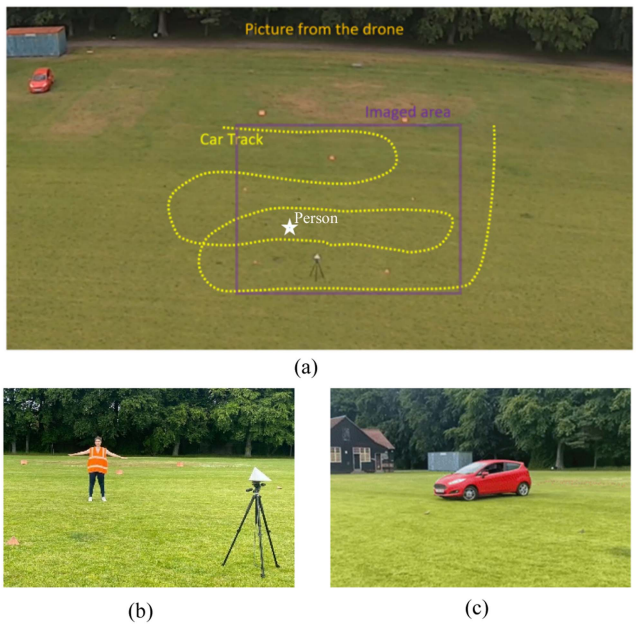

Fig. 18. Second scenario. (a) Scene. (b) Standing person during the first flight. (c) Moving car before the second flight.

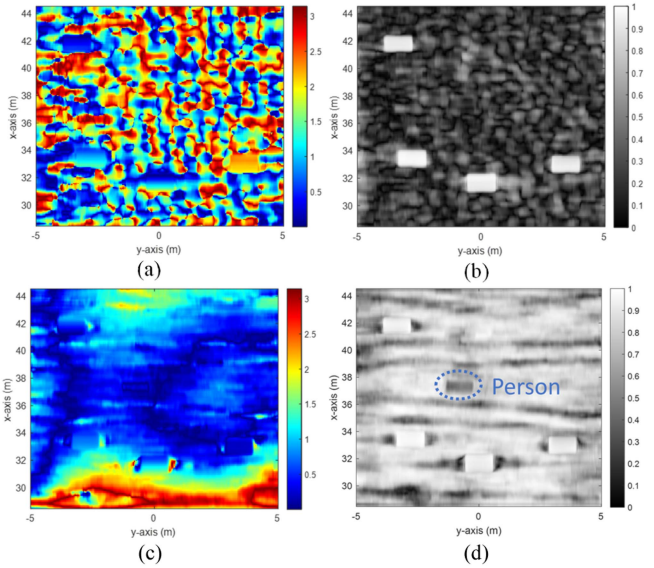

Fig. 19. (a) CCD phase before GA-based optimization. (b) CCD map before GA-based optimization. (c) CCD phase after GA-based optimization. (d) CCD map after GA-based optimization, where the x-axis represents the ground range, and the y-axis represents the cross-range.

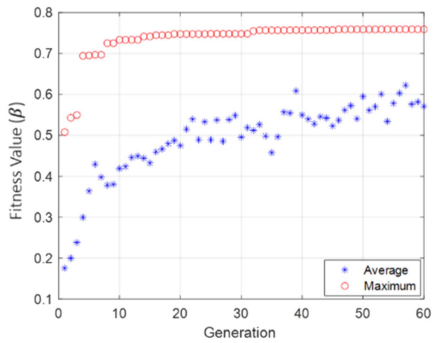

Fig. 20. GA processing: The mean fitness value of each generation is shown in blue and the individual who has the best fitness value in each generation is shown in red color.

B. Scenario II

In this part, a larger scene (15 m $\times$ 27 m) was considered [see Fig. 18(a)]. After presenting how to form a local change map in detail, an example of generating a bigger change map is illustrated. In the scenario, a person stands on grass as seen in Fig. 18(b) during the first flight. Before the second pass, the person is removed from the scene, and the track shown in Fig. 18(a) is followed by the car. A picture of the car can be seen in Fig. 18(c).

First, a local scene with a size of 10 m $\times$ 16 m is chosen, and the MoCo strategy presented in Section III is implemented. The selected local scene is the same as in the first scenario. After forming the primary and secondary images with a 6 cm azimuth and 40 cm ground-range resolution similar to the previous scenario, co-registration is done as described in Section III-A. At this point, if the coherence map and its phase are plotted based on (1) by using a 2 $\times$ 10 sliding window, Fig. 19(a) and (b) is obtained. As expected, point-like targets do not decorrelate, but the coherence map is distorted completely, and no change is visible due to phase errors. To maximize the coherency, the proposed method is used. As in the first scenario, the coefficients of the error function are estimated by the GA-based optimization method by using the same initial parameters except for the maximum iteration number P. Here, P is selected as 60 to see how much difference occurs compared to 30 iterations. As long as P increases, the probability of achieving higher coherencies increases. The improvement achieved by GA can be seen in Fig. 20. If the best individuals are examined in each generation (indicated by red circles), it is seen that the initial coherence is around 0.5. After creating 30 generations, the average coherence value of the best individual is obtained as 0.74, whereas, at the end of 60 generations, a 0.76 average coherence is achieved. The mean coherence value of each generation (in blue) experiences an increase as well and reaches up to 0.6 at the end of 60 generations.

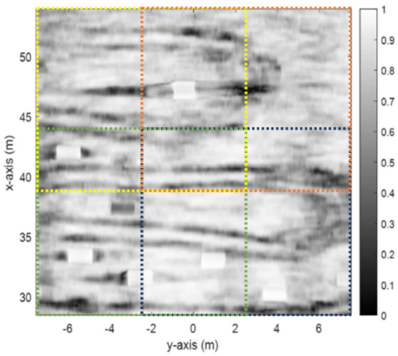

(a)

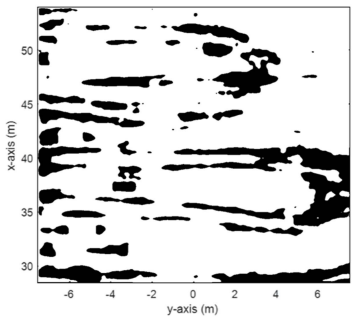

(b)

Fig. 21. (a) Final change map after the combination of the four subimages. (b) Result after applying a global image threshold using Otsu's method.

The result belonging to the best solution is shown in Fig. 19(c) and (d). Most of the phase errors are removed and as a result, the car tyre marks and the person who left the scene before the second flight are visible.

Moreover, subtle changes in a larger scene can be observed as described in Section III. The formed local change map shown in Fig. 19(d) is stored. Then, another subscene is selected, and the local change map for it is formed by applying the same CCD processing steps. After registering the formed local maps, larger change maps can be generated as in Fig. 21. In this example, four subimages that were half-overlapped along the azimuth direction and 30% overlapped along the ground-range direction are used. The subscenes are shown with dashed rectangles in different colors in Fig. 21(a). Also, the obtained result can be seen in this figure. Apparently, besides aligning all the subscenes correctly, the algorithm is able to discern the car track including its turns. Our approach to choosing the overlapped part is to use the local change map that has a higher average coherence for the corresponding overlapped part.

The detection result after applying a threshold to the CCD map in Fig. 21(a) is shown in Fig. 21(b) in binary form. Here, the threshold is determined by using Otsu's method, which is based on minimizing the intraclass variance of the black-and-white pixels [33]. The figure proves that even using a simple threshold, the car track and the standing person can be detected.

V. Discussion

The results given in Section IV show the ability of the drone-borne SAR system to change detection and validate the approach proposed in Section III. Subtle changes on a grass floor (grass length less than 2.5 cm) that are indistinguishable by the eye are observed on the generated change maps by using a high-frequency, high-resolution drone-borne SAR system. Human footprints appear with a 0.65 average coherence value in Fig. 16(d) that has 0.81 average coherence value whereas, car tyre marks are observed with less than 0.5 average coherence in Fig. 19(d) that has 0.76 average coherence value. Although we can detect changes, the local change maps generated may have different intensities. This is evident in Fig. 21(a), where the intensity of each local change map varies. The fundamental reason for having different intensities is having different image quality factors. Even if the local scene size is determined accordingly to minimize spatially variant phase errors in the local scene, some residual phase errors may exist in it. Furthermore, applying LQMD and PGA may result in random azimuth offsets for each individual SAR image, which may exaggerate processing decorrelation. Another reason could be co-registration quality. The co-registration method used in this work considers errors arising from translation, rotation, scale, and shear. If the local image pair has a different kind of error, this degrades the change detection result. Moreover, the GA-based optimization technique employed to minimize the phase errors between the image pair uses a parametric model that estimates errors up to the second order. Hence, higher-order phase errors can decrease the performance of the algorithm. As a result, having different change detection performances for each local scene is a natural consequence of the image formation and change map generation processes. Nevertheless, as a proof-of-concept, this work shows that drone-borne SAR change maps can be reasonably formed.

VI. Conclusion

In this article, it is shown, for the first time, that a high-frequency, high-resolution drone-borne SAR system operating at short ranges is capable and possible of detecting subtle changes, such as human footprints or car tyre marks, on a grass floor. After evaluating the decorrelation sources and limitations of the drone-borne SAR system built in-house, a CCD algorithm that includes data-driven autofocus-aided SAR image formation, intensity-based image co-registration, and GA-based interferometric phase error compensation methods is proposed.

The performance of the CCD algorithm and the drone-borne SAR system is validated through experiments aimed at detecting human footprints and car tyre marks. As a result, higher than 0.75 average coherence between the drone-borne SAR images is achieved, which makes it possible to form drone-borne SAR CCD maps with an mm-level sensitivity.

This work and the results presented in this article demonstrate that drone-borne SAR systems have great potential to be used for monitoring and security applications. On the other hand, the performance is sensitive to the selection of the local scene size and co-registration quality. The results with the baseline system show clear potential, but further areas for research to further improve capability are identified. These include making the local scene size determination automatic based on image quality factors, improving the image co-registration performance by employing nonglobal and nonlinear transformation models, and including an adaptive polynomial order model to remove residual CCD phase errors.

REFERENCES

[1] L. Miccinesi, A. Beni, and M. Pieraccini, "UAS-borne radar for remote sensing: A review," *Electronics*, vol. 11, 2022, Art. no. 3324.

[2] Y. Á. López, M. García-Fernández, G. Álvarez-Narciandi, and F. L.-H. Andrés, "Unmanned aerial vehicle-based ground-penetrating radar systems: A review," *IEEE Geosci. Remote Sens. Mag.*, vol. 10, no. 2, pp. 66–86, Jun. 2022.

[3] S. Zhou, L. Yang, L. Zhao, and G. Bi, "Quasi-polar-based FFBP algorithm for miniature UAV SAR imaging without navigational data," *IEEE Trans. Geosci. Remote Sens.*, vol. 55, no. 12, pp. 7053–7065, Dec. 2017.

[4] Z. Xu and D. Zhu, "High-resolution miniature UAV SAR imaging based on GPU architecture," *J. Phys., Conf. Ser.*, vol. 1074, Sep. 2018, Art. no. 012122.

[5] M. Lort, A. Aguasca, C. López-Martínez, and T. M. Marín, "Initial evaluation of SAR capabilities in UAV multicopter platforms," *IEEE J. Sel. Topics Appl. Earth Observ. Remote Sens.*, vol. 11, no. 1, pp. 127–140, Jan. 2018.

[6] M.-L. Ding, C.-B. Ding, L. Tang, X.-M. Wang, J.-M. Qu, and R. Wu, "A W-band 3-D integrated mini-SAR system with high imaging resolution on UAV platform," *IEEE Access*, vol. 8, pp. 113601–113609, 2020.

[7] A. Bekar, M. Antoniou, and C. J. Baker, "High-resolution drone-borne SAR using off-the-shelf high-frequency radars," in *Proc. IEEE Radar Conf.*, 2021, pp. 1–6.

[8] A. Bekar, M. Antoniou, and C. J. Baker, "Low-cost, high-resolution, drone-borne SAR imaging," *IEEE Trans. Geosci. Remote Sens.*, vol. 60, 2022, Art. no. 5208811.

[9] O. Frey and C. L. Werner, "UAV-borne repeat-pass SAR interferometry and SAR tomography with a compact L-band SAR system," in *Proc. 13th Eur. Conf. Synthetic Aperture Radar*, 2021, pp. 1–4.

[10] G. Oré et al., "Crop growth monitoring with drone-borne DInSAR," *Remote Sens.*, vol. 12, no. 4, Feb. 2020, Art. no. 615.

[11] G. Oré et al., "Predicting sugarcane harvest date and productivity with a drone-borne tri-band SAR," *Remote Sens.*, vol. 14, no. 7, Apr. 2022, Art. no. 1734.

[12] D. Luebeck et al., "Drone-borne differential SAR interferometry," *Remote Sens.*, vol. 12, no. 5, Feb. 2020, Art. no. 778.

[13] C. V. Jakowatz Jr., D. E. Wahl, P. H. Eichel, D. C. Ghiglia, and P. A. Thompson, *Spotlight-mode Synthetic Aperture Radar: A Signal Processing Approach*. Norwell, MA, USA: Kluwer, 1996.

[14] D. G. Corr and A. Rodrigues, "Coherent change detection of vehicle movements," in *Proc. Sens. Manag. Environ., IEEE Int. Geosci. Remote Sens. Symp. Proc.*, 1998, pp. 2451–2453.

[15] M. L. Williams and M. Preiss, "Physics-based predictions for coherent change detection using X-band synthetic aperture radar," *EURASIP J. Adv. Signal Process.*, vol. 2005, no. 20, pp. 3243–3258, Dec. 2005.

[16] M. Cha, R. D. Phillips, P. J. Wolfe, and C. D. Richmond, "Two-stage change detection for synthetic aperture radar," *IEEE Trans. Geosci. Remote Sens.*, vol. 53, no. 12, pp. 6547–6560, Dec. 2015.

[17] M. Preiss, D. A. Gray, and N. J. S. Stacy, "Detecting scene changes using synthetic aperture radar interferometry," *IEEE Trans. Geosci. Remote Sens.*, vol. 44, no. 8, pp. 2041–2054, Aug. 2006.

[18] D. E. Wahl, D. A. Yocky, C. V. Jakowatz, and K. M. Simonson, "A new maximum-likelihood change estimator for two-pass SAR coherent change detection," *IEEE Trans. Geosci. Remote Sens.*, vol. 54, no. 4, pp. 2460–2469, Apr. 2016.

[19] M. Wang, G. Huang, J. Zhang, F. Hua, and L. Lu, "A weighted coherence estimator for SAR coherent change detection," *IEEE Trans. Geosci. Remote Sens.*, vol. 60, 2022, Art. no. 5228912.

[20] A. Bekar, M. Antoniou, and C. J. Baker, "Change detection for high-resolution drone-borne SAR at high frequencies - First results," in *Proc. IEEE Radar Conf.*, 2023, pp. 1–5.

[21] H. A. Zebker and J. Villasenor, "Decorrelation in interferometric radar echoes," *IEEE Trans. Geosci. Remote Sens.*, vol. 30, no. 5, pp. 950–959, Sep. 1992.

[22] I. G. Cumming and F. H. Wong, *Digital Processing of Synthetic Aperture Radar Data*. Norwood, MA, USA: Artech House, 2005.

[23] G. W. Hart, S. Levy, and R. McLenaghan, "Geometry," in *CRC Standard Mathematical Tables and Formulae*, D. Zwillinger, Ed. Boca Raton, FL, USA: CRC, 1995.

[24] B. Zitova and J. Flusser, "Image registration methods: A survey," *Image Vis. Comput.*, vol. 21, no. 11, pp. 977–1000, Oct. 2003.

[25] D. Loeckx, P. Slagmolen, F. Maes, D. Vandermeulen, and P. Suetens, "Nonrigid image registration using conditional mutual information," *IEEE Trans. Med. Imag.*, vol. 29, no. 1, pp. 19–29, Jan. 2010.

[26] F. Maes, A. Collignon, D. Vandermeulen, G. Marchal, and P. Suetens, "Multimodality image registration by maximization of mutual information," *IEEE Trans. Med. Imag.*, vol. 16, no. 2, pp. 187–198, Apr. 1997.

[27] D. Mattes, D. R. Haynor, H. Vesselle, T. Lewellen, and W. Eubank, "Non-rigid multimodality image registration," in *Proc. Med. Imag., Image Process.*, 2001, pp. 1609–1620.

[28] M. Styner, C. Brechbuehler, G. Székely, and G. Gerig, "Parametric estimate of intensity inhomogeneities applied to MRI," *IEEE Trans. Med. Imag.*, vol. 19, no. 3, pp. 153–165, Mar. 2000.

[29] H.-S. Jung, J.-S. Won, and S.-W. Kim, "An improvement of the performance of multiple-aperture SAR interferometry (MAI)," *IEEE Trans. Geosci. Remote Sens.*, vol. 47, no. 8, pp. 2859–2869, Aug. 2009.

[30] B. Xu, Z.-W. Li, Q.-J. Wang, M. Jiang, J.-J. Zhu, and X.-L. Ding, "A refined strategy for removing composite errors of SAR interferogram," *IEEE Geosci. Remote Sens. Lett.*, vol. 11, no. 1, pp. 143–147, Jan. 2014.

[31] J. H. Holland et al., *Adaptation in Natural and Artificial Systems: An Introductory Analysis With Applications to Biology, Control, and Artificial Intelligence*. Cambridge, MA, USA: MIT Press, 1992.

[32] J. De and K. Alan, *An Analysis of the Behavior of a Class of Genetic Adaptive Systems*. Minneapolis, MN, USA: Univ. Michigan Press, 1975.

[33] N. Otsu, "A threshold selection method from gray-level histograms," *IEEE Trans. Syst., Man, Cybern.*, vol. 9, no. 1, pp. 62–66, Jan. 1979.

Ali Bekar received the B.Sc. degrees in electrical and electronics engineering and mechanical engineering from Erciyes University, Kayseri, Türkiye, in 2015 and 2016, respectively, the M.Sc. degree in RF and microwave engineering, and the Ph.D. degree in electrical, electronics, and computer engineering from the University of Birmingham, Birmingham, U.K., in 2018 and 2023, respectively.

His research interests include synthetic aperture radar (SAR) processing, drone-borne SAR imaging, and MIMO radar.

Muge Bekar received the B.S. degrees in electrical-electronics engineering and mechanical engineering from Erciyes University, Kayseri, Türkiye, in 2015 and 2016, respectively, the M.Sc. degree in RF and microwave engineering from the University of Birmingham, Birmingham, U.K., in 2018, where she is currently working toward the Ph.D. degree in electrical, electronics, and computer engineering with the Microwave Integrated Systems Laboratory (MISL).

Her research interests include sub-THz automotive radar, dual radar and communication systems, MIMO antenna design, and superresolution techniques.

Christopher J. Baker (Fellow, IEEE) is currently a Professor of Radar Research with the Electronic and Electrical Engineering Department, University College London, London, U.K. He has been actively engaged in radar system research since 1984 and is the author of more than 100 publications. His research interests include coherent radar techniques, radar signal processing, radar signal interpretation, electronically scanned radar systems, and radar imaging.

Prof. Baker is a Fellow of the IEE. He is currently the Chairman of the IEE Radar, Sonar and Navigation system's professional network. He is the recipient of the IEE Mountbatten premium (twice), and the IEE Institute premium.

Michail Antoniou (Senior Member, IEEE) received the B.Eng. (Hons.) degree in electronic and communications engineering and the Ph.D. degree in radar sensors and systems from the University of Birmingham, Birmingham, U.K., in 2003 and 2007, respectively.

From 2006 to 2011, he was a Research Fellow with the Microwave Integrated Systems Laboratory, University of Birmingham. Since 2011, he has been with the Department of Electronic, Electrical and Systems Engineering, University of Birmingham, where he is currently a Reader in RF sensing systems. His research interests include passive radar, SAR processing, multistatic and MIMO radar, and cognitive radar. He has authored or coauthored more than 100 publications in peer-reviewed international journals and conferences in these research areas.